

The Conversion Chemistry for High-Energy Cathodes of Rechargeable Sodium Batteries

Yongseok Lee,^{†,‡} Jung-Keun Yoo,^{‡,§} Jae Hyeon Jo,[†] Hyunyoung Park,[†] Chang-Heum Jo,[†] Wonseok Ko,[†] Hitoshi Yashiro,[§] Seung-Taek Myung,^{*,†,§} and Jongsoo Kim^{*,†,§}

[†]Department of Nanotechnology and Advanced Materials Engineering & Sejong Battery Institute, Sejong University, Seoul 05006, Republic of Korea

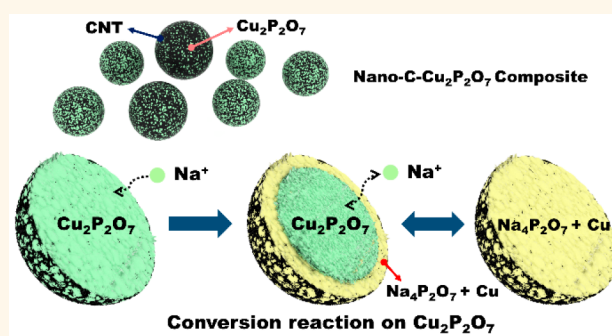
[‡]Carbon Composites Department, Composites Research Division, Korea Institute of Materials Science (KIMS), 797 Changwondaero, Changwon, Republic of Korea

[§]Department of Chemistry and Bioengineering, Iwate University, 4-3-5 Ueda, Morioka, Iwate 020-8551, Japan

Supporting Information

ABSTRACT: Herein, the $\text{Cu}_2\text{P}_2\text{O}_7$ /carbon–nanotube nanocomposite is reported as a cathode material based on a conversion reaction for rechargeable sodium batteries (RSBs). The nanocomposite electrode exhibits the large capacity of 355 mAh g^{-1} , which is consistent with the 4 mol Na^+ storage per formula unit determined by first-principles calculation. Its average operation voltage is approximately 2.4 V (vs Na^+/Na). Even at 1800 mA g^{-1} , a capacity of 223 mAh g^{-1} is maintained. Moreover, the composite electrode exhibits acceptable capacity retention of over 75% of the initial capacity for 300 cycles at 360 mA g^{-1} . The overall conversion reaction mechanism on the $\text{Cu}_2\text{P}_2\text{O}_7$ /carbon–nanotube nanocomposite is determined to be $\text{Cu}_2\text{P}_2\text{O}_7 + 4\text{Na}^+ + 4\text{e}^- \rightarrow 2\text{Cu} + \text{Na}_4\text{P}_2\text{O}_7$ based on *operando/ex situ* structural and physicochemical analyses. The high energy density of the $\text{Cu}_2\text{P}_2\text{O}_7$ /carbon–nanotube nanocomposite (720 Wh kg^{-1}) supported by this conversion chemistry indicates a high possibility of application of this material as a promising cathode candidate for RSBs.

KEYWORDS: $\text{Cu}_2\text{P}_2\text{O}_7$, first-principles calculation, conversion, cathode, sodium, battery



To reduce the environmental burden arising from usage of fossil fuels, it is essential to develop energy storage systems (ESSs) for efficient storage of the electricity generated by power plants and renewable-energy generation systems.^{1–7} The merits of Li-ion batteries (LIBs), such as high energy density, acceptable power capability, and stable cycle life, make them particularly attractive ESS candidates for various power sources.^{8–13} However, the recent explosive growth of LIBs has contributed to the fluctuating prices of lithium resources, which have in turn increased the production cost of LIBs.^{14–18}

Rechargeable sodium batteries (RSBs) are considered promising alternatives to LIBs, owing to abundant Na resources in the sea and similar alkali-ion-based reaction mechanisms of RSBs with LIBs, which adopt de/intercalation,¹⁹ conversion,²⁰ and de/alloying processes.²¹ However, the slightly higher standard electrode potential of Na (−2.71 V vs a standard hydrogen electrode (SHE)) than that of Li (−3.04 V vs SHE) may negate the merits of RSBs,^{22–24} provided that the delivered specific capacity is similar to that of a LIB electrode. Thus, to compensate for the low energy

density of RSBs, the capacities of cathode materials for RSBs must be higher than those for LIBs.^{25–32}

Conversion-based electrode materials generally have large capacities; however, their main electrochemical reaction occurs at low voltage, leading to the application of these materials mainly as anodes.^{33,34} Nevertheless, provided that the operation voltage can be increased, these conversion-based electrode materials could potentially be applied as cathode materials because of their large capacities. One possible approach is the use of polyanion frameworks with high electronegativity (resulting from the inductive effect) to increase the redox potentials of transition metal (TM) ions.^{35–38} In addition, Cu-based compounds have been reported to have less negative values of standard enthalpy of formation than other TM-based compounds, indicating the feasibility of achieving a higher redox potential by using Cu-based compounds.²²

Received: July 18, 2019

Accepted: October 10, 2019

Published: October 10, 2019

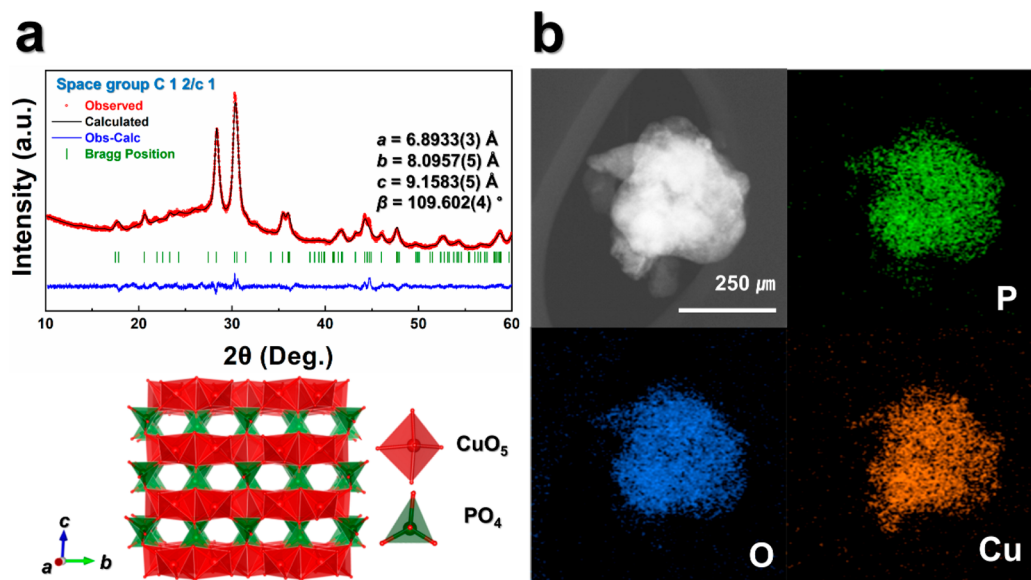


Figure 1. (a) Refined XRD pattern of nano-C-Cu₂P₂O₇ composite ($R_p = 2.2\%$, $R_l = 2.14\%$, $R_F = 1.35\%$, and $\chi^2 = 2.51\%$) and crystal structure of Cu₂P₂O₇. (b) Elemental analysis using EDS mapping (P: green, O: blue, Cu: orange) of nano-C-Cu₂P₂O₇ composite.

Table 1. Detailed Structural Information of nano-C-Cu₂P₂O₇ Obtained by Rietveld Refinement

atom	multiplicity	<i>x</i>	<i>y</i>	<i>z</i>	<i>B</i> _{iso}	occupancy
Cu1	8f	-0.0197(8)	0.3082(4)	0.5119(5)	1.26(4)	1
P1	8f	0.1979	0.0089(13)	0.2124(8)	0.80(11)	1
O1	4e	0	0.034(2)	0.25	0.35(13)	0.5
O2	8f	0.3711(16)	-0.006(2)	0.3511(14)	0.35(13)	1
O3	8f	0.2240(16)	0.148(2)	0.1134(15)	0.35(13)	1
O4	8f	0.1978(16)	-0.164(2)	0.1080(14)	0.35(13)	1

Inspired by polyanion frameworks and the associated inductive effect, we herein propose a conversion chemistry of Cu₂P₂O₇ in nonaqueous Na cells. The structural stability provided by the P–O polyanion framework makes this system more attractive than other systems such as S–O³⁹ and Si–O⁴⁰ systems, as demonstrated by the commercial success of LiFePO₄.^{35,36} We expected that the inductive effect originates from the stable P–O-based framework assisted by Cu, which has a negative value of standard enthalpy of formation, namely, that Cu₂P₂O₇ is stabilized in a monoclinic structure. Using first-principles calculations, we predicted the validity of the structural stability and electrochemical activity of Cu₂P₂O₇, which contribute to the conversion reaction Cu₂P₂O₇ + 4Na⁺ + 4e⁻ → 2Cu + Na₄P₂O₇. In addition, we attempted to improve the electrochemical activity of Cu₂P₂O₇ through nanosized compositization with carbon nanotubes (CNTs), namely, the formation of nano-C-Cu₂P₂O₇. The nano-C-Cu₂P₂O₇ electrode exhibited the large first discharge of 355 mAh g⁻¹, which is highly similar to the theoretical capacity of Cu₂P₂O₇ (corresponding to 4 mol Na storage per formula unit of Cu₂P₂O₇) between 1 and 4 V (vs Na⁺/Na) under the charge/discharge current of 12 mA g⁻¹. The feasibility of using nano-C-Cu₂P₂O₇ was further demonstrated by its capacity retention of 223 mAh g⁻¹ at a high current of 1800 mA g⁻¹. Moreover, the nano-C-Cu₂P₂O₇ retained over 75% of its initial capacity for 300 cycles at 360 mA g⁻¹. The predicted conversion reaction was elucidated using *operando* X-ray diffraction (XRD), high-resolution transmission electron microscopy (HRTEM), X-ray absorption near edge structure spectroscopy (XANES), and extended X-ray absorption fine

structure (EXAFS) spectroscopy analyses. Namely, we demonstrated that Cu₂P₂O₇ is converted into Cu⁰ metal and Na₄P₂O₇ during the sodiation process and recovered to Cu₂P₂O₇, though with low crystallinity, during the desodiation process.

RESULTS AND DISCUSSION

Through first-principles calculation, the theoretical redox potential (*V*) of Cu₂P₂O₇ in a Na cell was calculated as follows:

$$V = -\frac{2E(\text{Cu}) + E(\text{Na}_4\text{P}_2\text{O}_7) - E(\text{Cu}_2\text{P}_2\text{O}_7) - 4E(\text{Na})}{4F}$$

E(*x*) indicates the formation energies on *x* species, which is tabulated in Table S1. The theoretical average operation potential of Cu₂P₂O₇ is close to ~2.7 V (vs Na⁺/Na). This prediction implies that high operation voltage of Cu₂P₂O₇ under the RSB system is reasonable despite the conversion reaction. CuO is also predicted to be active by a conversion process (CuO + 2Na⁺ + 2e⁻ → Cu + Na₂O) and its average operation voltage is just ~1.2 V, which indicates that the resulting operation voltage of Cu₂P₂O₇ is thus higher than that of CuO. This finding is attributed to the presence of the P–O bond with high electronegativity in Cu₂P₂O₇. Varying the connecting element from O to the P–O polyanion is thus predicted to increase the operation voltage during the expected conversion reaction in Na cells.

Because the related conversion may progress sluggishly, reduction of the particle size together with modification by carbon or other electro-conducting media is necessary to

facilitate electron transfer by reducing the electron conduction path connecting active particles. The as-synthesized $\text{Cu}_2\text{P}_2\text{O}_7$ was thus subjected to high-energy ball milling with CNTs (1 wt % vs the active materials). The carbon content of the nano-C- $\text{Cu}_2\text{P}_2\text{O}_7$ composite was determined to be ~ 20 wt % (including CNTs) using thermogravimetric analysis (TGA) and the existence of carbon contents is also confirmed through Raman spectroscopy (Figure S1).⁴¹ The original crystal structure of $\text{Cu}_2\text{P}_2\text{O}_7$ with $C12/c1$ space group was maintained in the compositized product despite the high-energy ball-milling process used for nanosizing and CNT mixing (Figure S2). Through structural analyses using Rietveld refinement, we verified that the lattice parameters of the compositized nano-C- $\text{Cu}_2\text{P}_2\text{O}_7$ were $a = 6.8933(3)$ Å, $b = 8.0957(5)$ Å, $c = 9.1583(5)$ Å, and $\beta = 109.602^\circ(4)$ (Figure 1a and Table 1), which is well matched with those of the as-synthesized $\text{Cu}_2\text{P}_2\text{O}_7$ (Table S2) and the values reported in the literature.^{42–44} The crystal structure of $\text{Cu}_2\text{P}_2\text{O}_7$ determined from the Rietveld refinement was further visualized using transmission electron microscopy (TEM) analyses with energy-dispersive X-ray spectroscopy (EDS) mapping, demonstrating that the nano-C- $\text{Cu}_2\text{P}_2\text{O}_7$ was composed of C, Cu, P, and O elements (Figure 1b). Comparison of the morphologies of the nano-C- $\text{Cu}_2\text{P}_2\text{O}_7$ and fresh $\text{Cu}_2\text{P}_2\text{O}_7$ (Figure S2b and c) indicates that the particle size of $\text{Cu}_2\text{P}_2\text{O}_7$ is highly reduced after compositization by high-energy ball-milling. Table 2 shows that the average size on the

Table 2. Crystal Size of C- $\text{Cu}_2\text{P}_2\text{O}_7$ Composite Determined Using Scherrer Equation for Selected $h k l$ Reflections of XRD Pattern

peak position (2θ) _(hkl)	fwhm β_{size} (deg)	crystallite size (nm)
17.44 ₍₁₁₀₎	1.90	4.19
20.52 ₍₀₀₂₎	2.64	3.03
28.23 ₍₂₀₂₎	0.88	9.21
30.14 ₍₀₂₂₎	0.71	11.31
35.30 ₍₂₂₀₎	2.08	3.95
41.74 ₍₀₀₄₎	2.44	3.45
44.06 ₍₁₃₂₎	1.20	8.99

$K = 0.89$, $\lambda = 1.54178$ (Å), Average crystallite size = 6.41(nm)

$\text{Cu}_2\text{P}_2\text{O}_7$ crystalline at the nano-C- $\text{Cu}_2\text{P}_2\text{O}_7$ composite was calculated to be ~ 6.41 nm using the Scherrer equation. It was expected that sluggish kinetics of the conversion reaction of $\text{Cu}_2\text{P}_2\text{O}_7$ may be overcome by the nanosizing and CNT mixing, which could enlarge the surface area of $\text{Cu}_2\text{P}_2\text{O}_7$ and improve its electrical conductivity. The nano-C- $\text{Cu}_2\text{P}_2\text{O}_7$ electrodes were galvanostatically measured with a current of 12 mA g^{-1} in the Na cell system. As observed in Figure 2a and b, the nano-C- $\text{Cu}_2\text{P}_2\text{O}_7$ electrode delivered a first discharge capacity of 355 mAh g^{-1} , corresponding to 4 mol Na storage per formula unit of $\text{Cu}_2\text{P}_2\text{O}_7$. The observed operation voltage (2.4 V on average) was consistent, implying the occurrence of a conversion reaction, which is higher than that of other conversion-based electrode materials for RSBs^{20,45–47} but similar to that of intercalation-based cathode materials for RSBs.^{48–50} Despite the conversion reaction generally suffering from slow kinetics, the nano-C- $\text{Cu}_2\text{P}_2\text{O}_7$ can deliver a large capacity of approximately 223 mAh g^{-1} even at 5C ($1\text{C} = 355 \text{ mA g}^{-1}$), which is $\sim 63\%$ of the capacity at 12 mA g^{-1} . We supposed that faster capacity deterioration at the high current

rate may result from the large overpotential and acceleration of the electrolyte decomposition. In particular, it was verified that the nano-C- $\text{Cu}_2\text{P}_2\text{O}_7$ delivered average operation voltages of ~ 2.7 V on charge and ~ 2.1 V on discharge and. Moreover, the nano-C- $\text{Cu}_2\text{P}_2\text{O}_7$ retained over 75% of its initial capacity with a high Coulombic efficiency for 300 cycles at 360 mA g^{-1} (Figure 2c). In addition, to investigate the reasons for the capacity fading after 100 cycles and the difference between the charge/discharge capacities, we compared crystal structure and morphology between the as-prepared electrode and the 100-cycled electrode through TEM, SEM, and XRD analyses. As presented in Figures S3–5, despite the $100\times$ repeated charge/discharge, morphological and structure changes were not observed, which implies that the capacity fading after 100 cycles may result from the electrolyte decomposition and other side reactions. Furthermore, the morphologies and crystal structure of nano-C- $\text{Cu}_2\text{P}_2\text{O}_7$ were well retained without severe degradation over 300 cycles in the Na cell system (Figures S3–5). It is supposed that homogeneous mixing of conductive carbons such as CNT may result in suppression of severe structural degradation during repeated charge/discharge, which is connected to good cycle performances of nano-C- $\text{Cu}_2\text{P}_2\text{O}_7$ electrode over 300 cycles. In addition, as presented in Figure S6, the nano- $\text{Cu}_2\text{P}_2\text{O}_7$ without carbon mixing just exhibited poor cycle performance at the same experimental conditions as nano-C- $\text{Cu}_2\text{P}_2\text{O}_7$. We supposed that the continuous carbon-mixing process through high-energy ball-milling highly enhanced the cyclability of $\text{Cu}_2\text{P}_2\text{O}_7$ despite conversion reaction. As shown in Figure 3a,b, a full cell was fabricated with $\text{Cu}_2\text{P}_2\text{O}_7$ and presodiated hard carbon electrodes.⁵¹ The full cell was tested for 100 cycles at C/3 at the voltage range between 0.9 and 3.9 V. It exhibited acceptable performance, such as a first discharge capacity of 283 mAh g^{-1} and more than 81% capacity retention of the initial capacity for 100 cycles at C/3. Moreover, we calculated the full cell capacity based on cell-level mass using the following reaction

$$C_{\text{full}} = \frac{1}{\frac{1}{C_c} + \frac{1}{C_a}} = \frac{C_a C_c}{C_a + C_c}$$

where C_{full} , C_c , and C_a are the specific capacities of the full cell, cathode, and anode, respectively.⁵² Because C_a and C_c are $\sim 297 \text{ mAh g}^{-1}$ and $\sim 294 \text{ mAh g}^{-1}$, respectively, the calculated C_{full} is $\sim 148 \text{ mAh g}^{-1}$. Figure S7 below shows the full-cell capacity of nano-C- $\text{Cu}_2\text{P}_2\text{O}_7$ /hard carbon based on the cell-level mass.

In addition, based on the integral of each discharge curve (vs voltage), we calculated the energy densities and drew the Ragone plot with comparison of not only conversion-based materials but also intercalation-based materials (Figure 4). It was verified that nano-C- $\text{Cu}_2\text{P}_2\text{O}_7$ exhibits better electrochemical performances than other conversion-based^{48,53–56} and intercalation-based^{25,57–60} cathode materials for RSBs with large specific capacity ($\geq 180 \text{ mAh g}^{-1}$). To verify the particle-size effect on the electrochemical performances of $\text{Cu}_2\text{P}_2\text{O}_7$, we compared the charge-transfer resistance and rate-capability between pristine $\text{Cu}_2\text{P}_2\text{O}_7$ having large crystalline size ($\geq \sim 1 \mu\text{m}$) and nano-C- $\text{Cu}_2\text{P}_2\text{O}_7$. As presented in Figure S8, through the EIS analyses, it was verified that the nano-C- $\text{Cu}_2\text{P}_2\text{O}_7$ exhibited much lower charge-transfer resistance than the pristine $\text{Cu}_2\text{P}_2\text{O}_7$, which indicates the improved electrical conductivity of $\text{Cu}_2\text{P}_2\text{O}_7$ achieved through nanosizing and

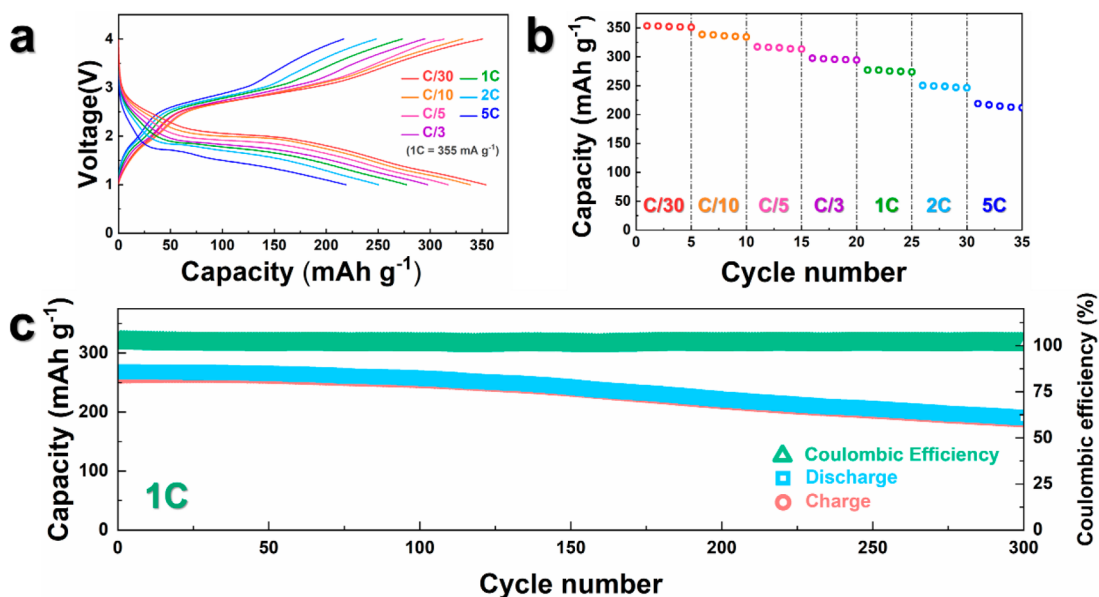


Figure 2. (a) Charge/discharge curves of nano-C-Cu₂P₂O₇ at various current rates. (b) Rate cycling performance of nano-C-Cu₂P₂O₇ composite from C/30 to 5C. (c) Cyclic performance and Coulombic efficiency of nano-C-Cu₂P₂O₇ during 300 cycles at 1C after 1 cycle at C/3.

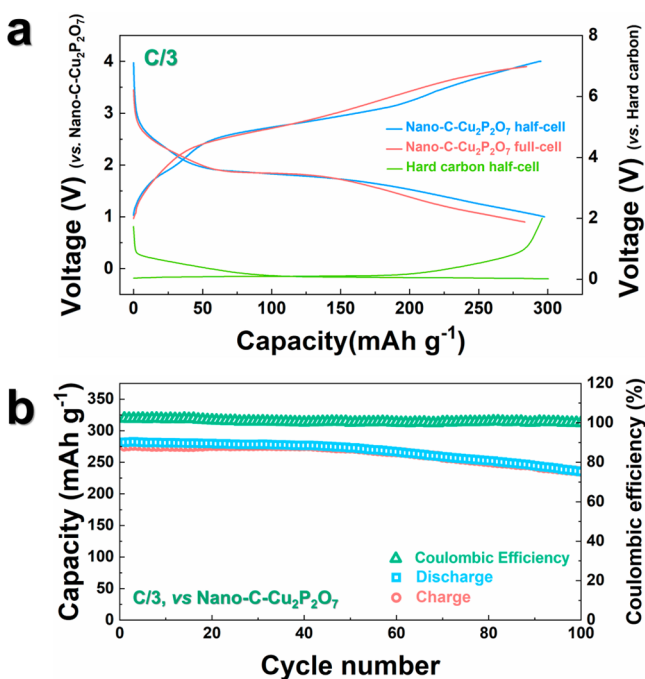


Figure 3. (a) Charge/discharge profiles of nano-C-Cu₂P₂O₇ half-cell, full cell, and hard carbon half-cell of initial cycle at C/3. (b) Cyclic performance and Coulombic efficiency of nano-C-Cu₂P₂O₇ full cell over 100 cycles at C/3.

CNT mixing. Furthermore, it was verified that the pristine Cu₂P₂O₇ with large crystalline size exhibited insufficient electrochemical performance with low capacities at the same experimental condition and the same carbon contents as the nano-C-Cu₂P₂O₇ (Figure S9). Through these experimental results, we confirmed that it is very hard to achieve the theoretical capacity of Cu₂P₂O₇ without the nanoeffect and homogeneous carbon-mixing. It was reported that conversion-based electrode materials have poor electrical conductivity due to a large band gap and long ionic diffusion length.^{61,62} The

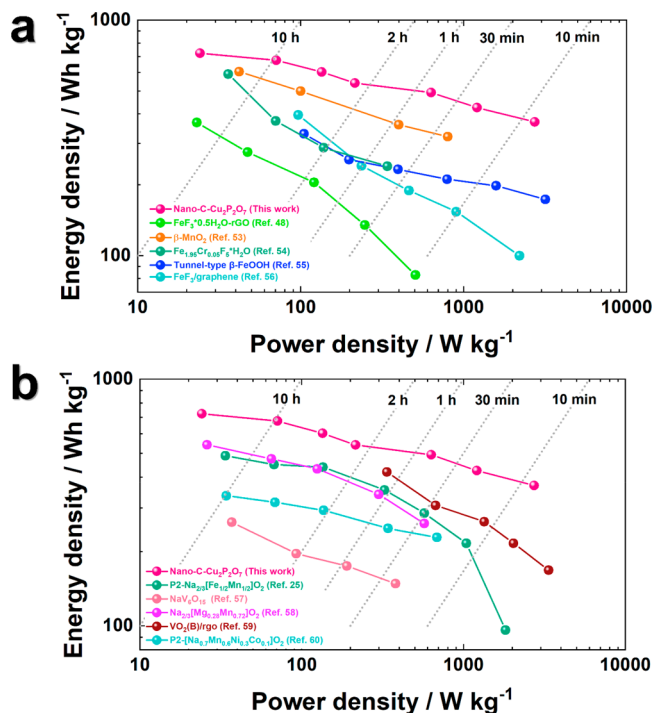


Figure 4. Ragone plot on the nano-C-Cu₂P₂O₇ and other (a) conversion-based and (b) intercalation-based cathode materials for RSBs with high specific capacity (>180 mAh g⁻¹).

relationship between diffusion time (τ) and the diffusion length of Na ions (L_{Na}) is as follows:

$$\tau = L_{\text{Na}}^2 / D_{\text{Na}}$$

D_{Na} means diffusion coefficient on Na ions. At the equation, the diffusion time is greatly reduced with the decrease in diffusion length, which means that the shortened diffusion path causes fast Na⁺ diffusion, and then, the electrochemical performance is highly enhanced. Furthermore, the homoge-

neous coating of conductive carbon results in highly enhanced electronic conductivity, which enables an improved power capability of active material through effective diffusion of electrons.^{63–65}

To verify the conversion process predicted by the first-principles calculation, *operando* XRD analysis of a nano-C-Cu₂P₂O₇ electrode in a Na cell was performed. The nano-C-Cu₂P₂O₇ electrode was charged/discharged at the C/20 with the voltage range between 1.1 and 4.1 V (vs Na⁺/Na). As observed in Figure 5a,b, as sodiation (discharge) progressed,

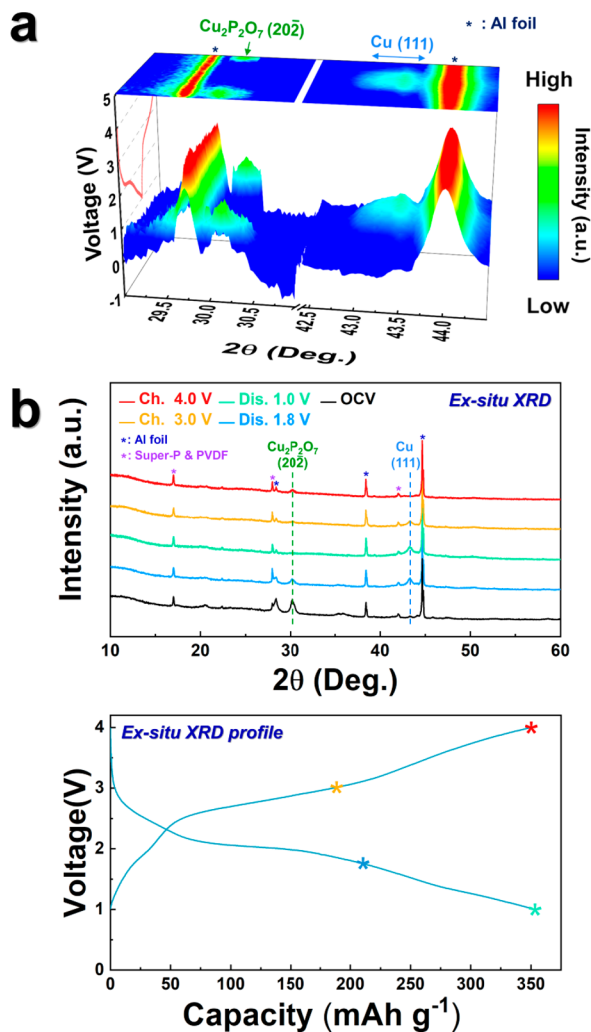


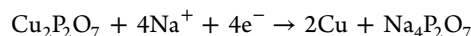
Figure 5. (a) *Operando* XRD patterns of nano-C-Cu₂P₂O₇ electrode during the first cycle. (b) *Ex situ* XRD patterns of nano-C-Cu₂P₂O₇ electrodes at various voltages and corresponding preparation process of nano-C-Cu₂P₂O₇ composite.

the Cu₂P₂O₇ phase disappeared and the metallic Cu⁰ phase grew at 43° (2θ). During desodiation to 4.0 V, the formed metallic Cu⁰ gradually disappeared and the original Cu₂P₂O₇ was recovered in the 2θ range between 29° and 30°, indicating that the related reaction is highly reversible. Time-of-flight secondary-ion mass spectroscopy (ToF-SIMS) was used to identify the species produced after de/sodiation of the nano-C-Cu₂P₂O₇ electrodes (Figure 6). Because surface contaminants, mainly organic compounds composed of C–H–O bonds, originated electrolyte and sample treatment in air were observed on the surface of electrodes, the surface was etched

by Ga⁺ for 10 s to clean up the surface, as presented at Figure S10a. Since high energy is applied onto the substances, the secondary ions produced are subject to flying toward the detector, and they appear as positive and negative ions (Figure 6). The positive or negative secondary ion fragments demonstrate the presence of substances. In Figure S10b, ToF-SIMS spectra obtained after Ga⁺ etching for 10 s; and Cu₂⁺, Na₂P₂⁻, and Na₃PO₂⁺ after de/sodiation are represented. For the fresh electrode, the observed Cu⁺ (*m* = 62.92, Figure 6a), NaP₂⁻ (*m* = 84.93, Figure 6b), and Na₂PO⁺ (*m* = 92.94, Figure 6c) fragments were negligible. During sodiation, these fragments appeared, and the resulting relative intensities were intensified at the end of discharge at 1.0 V. The increase of the NaP₂⁻ (*m* = 84.93) and Na₂PO⁺ (*m* = 92.94) fragments indicates the presence of a Na–P–O bond as a sodiation product, presumably Na₄P₂O₇. As observed in the *operando* and *ex situ* XRD patterns, the phase related to Na₄P₂O₇ was not visible, indicating the low crystallinity of the Na₄P₂O₇ phase (Figure 5). Furthermore, the Cu⁺ is the secondary ion fragment that was observed after Ga⁺ bombardment to the electrode samples. As a result, the observation of Cu⁺ means that the observed compound contains or is composed of Cu element. Although the intensity of Cu⁺ was weak for the fresh state (Figure 6a), the increased relative intensities of Cu⁺ fragment on sodiation (1.8 and 1.0 V) and desodiation (3.0 V) mean that the observed material is composed of Cu, which is consistent with the XRD pattern (shown in Figure 5a,b and Figure 8) that illustrates the presence of Cu metal at 1.8 and 1.0 V on discharge and at 3.0 V on charge. HRTEM analysis revealed the formation of not only the low-crystallinity Na₄P₂O₇ phase but also Cu⁰ after discharge to 1.0 V (Figure 7a,b), which is well matched with the ToF-SIMS data; namely, the Cu₂P₂O₇ phase was converted to a metallic Cu⁰ phase accompanying the formation of Na₄P₂O₇ as a byproduct.

For the accurate analyses of SAED patterns based on HRTEM analyses, we applied the information on the (*hkl*) planes of each phase having the relatively high scattering intensity based on the Inorganic Crystal Structure Database (ICSD), such as Cu₂P₂O₇ (ICSD # 157107), Na₄P₂O₇ (ICSD # 10370), and Cu (ICSD # 627113). On desodiation, the relative intensities of these fragments decreased at 3.0 V and became almost negligible at 4.0 V (end of charge), as also evidenced by the TEM finding that the original Cu₂P₂O₇ appeared at the end of charge (Figure 7c,d). Namely, the produced Na₄P₂O₇ and metallic Cu⁰ phases were recovered to the original Cu₂P₂O₇ phase, which is consistent with the *operando* and *ex situ* XRD results (Figure 5). Figure 8a shows that during charging/discharging, the average oxidation state of Cu varied between 0 and +2, corresponding to the redox reaction of Cu₂P₂O₇ between Cu²⁺ and metallic Cu⁰. Furthermore, Fourier transform (FT) analyses of the EXAFS spectra of Cu₂P₂O₇ verified the reversible formation and disappearance between Cu–O and Cu–Cu bonds during the charge/discharge (Figure 8b), which is consistent with the previous results on Cu²⁺–Cu⁰ conversion reaction.^{66,67}

As presented in Figure 9, these experimental results confirm the validity of the following theoretically postulated conversion reaction:



As demonstrated in Figure 2, the previously mentioned conversion reaction is highly reversible, such that the electrode can deliver over 75% of the initial capacity for 300 cycles.

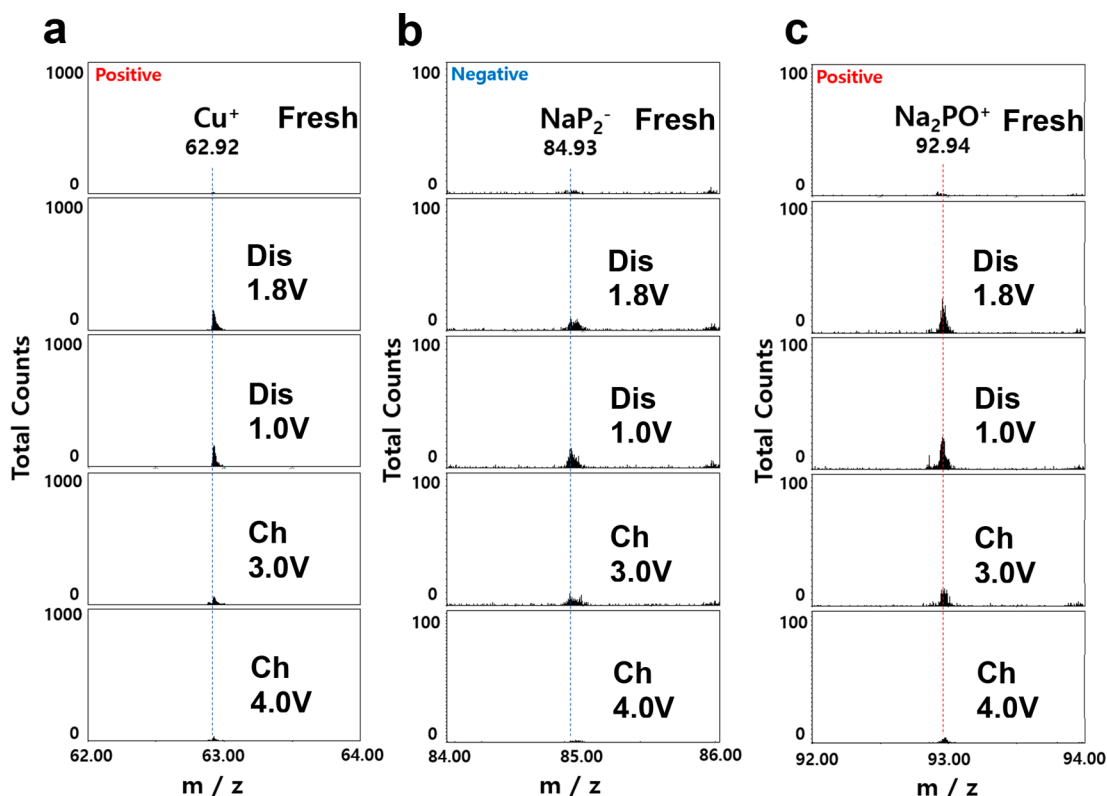


Figure 6. ToF-SIMS plots of (a) Cu^+ , (b) NaP_2O_7^- , and (c) Na_2PO^+ after de/sodiation.

Generally, conversion reactions cause volume expansion of electrodes via the formation of unwanted Na_xA_y (A: O, F, and S) during desodiation/sodiation. These continuous volume changes tend to cause exfoliation of active materials from the current collector, which results in loss of active materials and spontaneously reduces the capacity during cycling. Even though insulating $\text{Na}_4\text{P}_2\text{O}_7$ was produced by the conversion reaction, the product formed near the CNTs, which minimized the volume expansion of the electrode, making it possible to sustain the electrode morphology for long-term cyclability (Figures S3–5). Therefore, the CNT-assisted high electrical conductivity is responsible for the good reversibility of the conversion reaction even in the presence of $\text{Na}_4\text{P}_2\text{O}_7$, leading to the high Coulombic efficiency (approaching 100%), as observed in Figure 2c. More importantly, the formation of the $\text{Na}_4\text{P}_2\text{O}_7$ byproduct occurred at a high potential via the conversion reaction, as calculated. The nano-C- $\text{Cu}_2\text{P}_2\text{O}_7$ electrodes are thus suggested as a promising cathode material based on the conversion reaction for RSBs, providing large energy density of 720 Wh kg^{-1} .

CONCLUSION

In summary, we propose the application of nano-C- $\text{Cu}_2\text{P}_2\text{O}_7$ as a conversion cathode material for RSBs through our first-principles calculation predictions. The nano-C- $\text{Cu}_2\text{P}_2\text{O}_7$ electrode exhibits the large discharge capacity, $\sim 355 \text{ mAh g}^{-1}$, corresponding to the storage of 4 mol Na ions per formula unit. Moreover, the long-term cyclability is acceptable even at high rates. The $\text{Cu}_2\text{P}_2\text{O}_7$ undergoes a conversion reaction, leading to a high operation voltage via the inductive effect by forming $\text{Na}_4\text{P}_2\text{O}_7$. During discharge, $\text{Cu}_2\text{P}_2\text{O}_7$ converts into metallic Cu^0 and $\text{Na}_4\text{P}_2\text{O}_7$, and the Cu metal returns to the original $\text{Cu}_2\text{P}_2\text{O}_7$ during charge. We believe that adoption of

the inductive effect provides access to the chemistries lying dormant and has the positive effect of increasing the energy density of the active materials.

EXPERIMENTAL SECTION

Material Preparation. We prepared the crystalline $\text{Cu}_2\text{P}_2\text{O}_7$ powders using wet ball-milling process. Stoichiometric quantities of CuO (Sigma-Aldrich, 99%) and $\text{NH}_4\text{H}_2(\text{PO}_4)$ (Sigma-Aldrich, 98%) precursors were mixed at 300 rpm for 12 h with acetone. The obtained precursor was dried at 80°C for 10 h with stirring on a hot plate. The dried precursor was heated at 850°C for 10 h in air. The synthesized $\text{Cu}_2\text{P}_2\text{O}_7$ was mixed by high-energy ball milling of 80 wt % $\text{Cu}_2\text{P}_2\text{O}_7$ and 19 wt % Super P carbon black. The powders were placed in a nitride jar with 30 balls and mixed by ball-milling at 500 rpm for 15 h. Finally, the $\text{Cu}_2\text{P}_2\text{O}_7$ composition was mixed with 1 wt % CNTs using high-energy ball milling at 100 rpm for 12 h.

Material Characterization. We characterized the coated powders using XRD (PANalytical) with Cu $K\alpha$ radiation (wavelength = 1.54178 \AA). The 2θ range was 10° to 60° and applied time per step was 0.13. The XRD data was analyzed using the FullProf Rietveld program. SEM (SU-8010) and FESEM (JEM-2100F) were used to examine the morphology of the materials. Raman spectra were obtained using Raman spectroscopy (inVia, Renishaw) in the region of $200\text{--}3000 \text{ cm}^{-1}$. To analyze the byproducts on the surface of the active materials, the electrodes were examined by a time-of-flight secondary ion mass spectroscopy (ULVAC-PHI, ToF-SIMS PHI TRIFT V nanoTOF) surface analyzer operated at 10^{-9} Torr, and liquid Ga^+ ion source and pulse electron flooding were equipped. During the analysis, the targets were bombarded by the 10 keV Ga^+ beams from 0.3 to 0.5 pA of a pulsed primary ion current. The total collection time was 100 s, and an area of $400 \mu\text{m} \times 400 \mu\text{m}$ was rastered by beams. XANES spectroscopy was measured at the beamline 8D by the 3.0-GeV Pohang Light Source. A multichannel impedance analyzer system (Bio-Logic, VSP-300, Grenoble, France) from 5 MHz to 500 mHz was used to analyze the impedance of each sample.

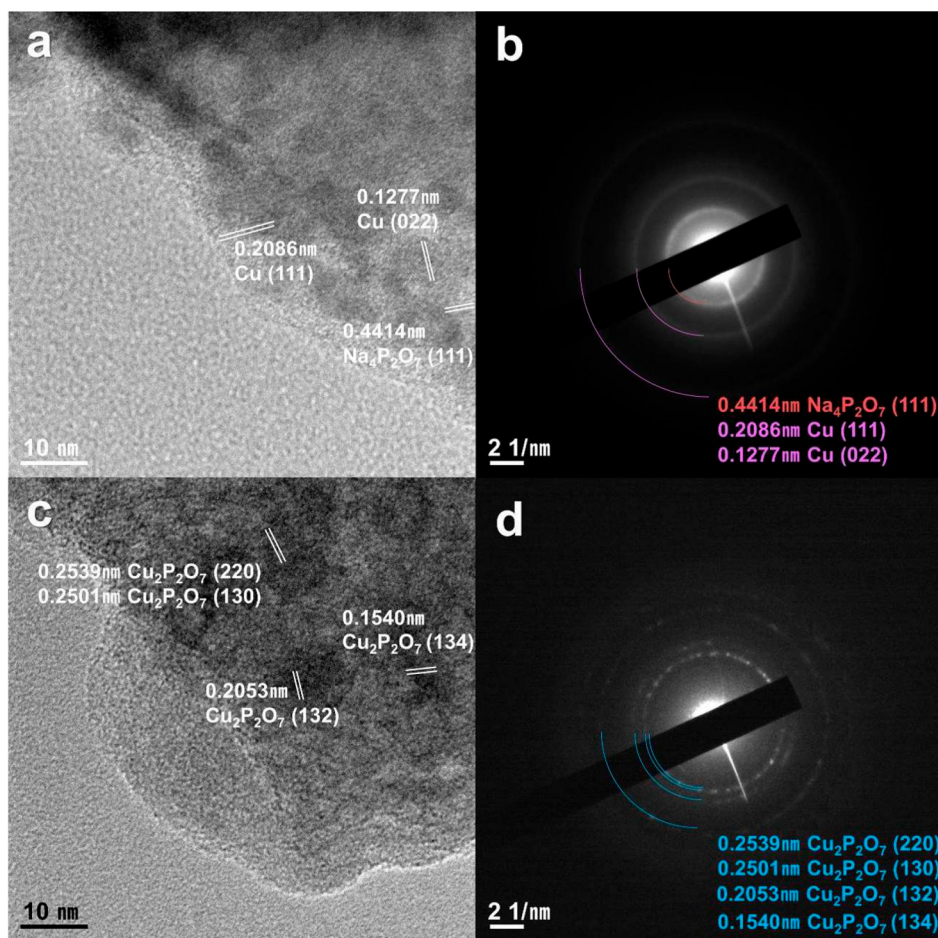


Figure 7. HRTEM images and SAED patterns of (a,b) discharged and (c,d) charged nano-C-Cu₂P₂O₇ composite.

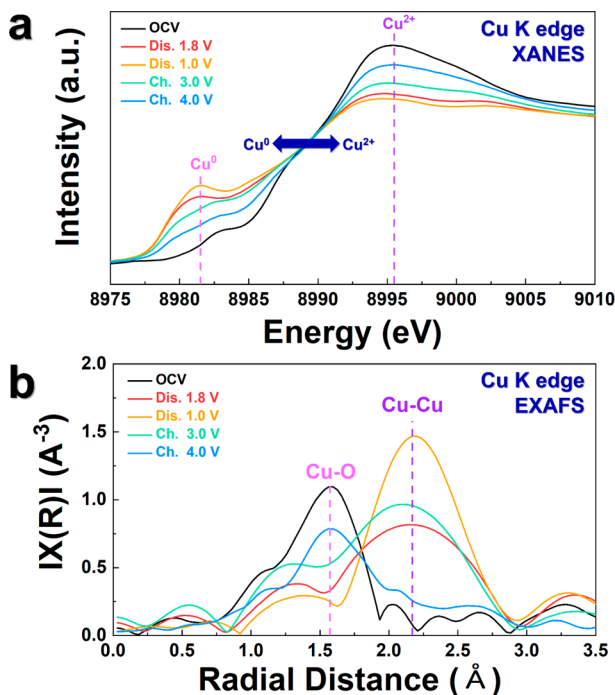


Figure 8. Cu K-edge (a) XANES and (b) EXAFS spectra of nano-C-Cu₂P₂O₇ samples.

Electrochemical Properties. The Cu₂P₂O₇ electrodes were fabricated from a slurry of the Cu₂P₂O₇ active material (80 wt % Cu₂P₂O₇, 19 wt % Super P carbon black, and 1 wt % CNT) and polyvinylidene fluoride (10 wt %) in *N*-methyl-2-pyrrolidone (NMP). The slurry was covered using a doctor blade on Al foil and dried in a vacuum oven for 12 h. R2032 cells were assembled using the Cu₂P₂O₇ electrode with a Na counter electrode in Ar glovebox. 1 M NaPF₆ in DMC:EC:FEC (49:49:2 v/v/v) was used as the electrolyte. We measured the electrochemical properties of the cells at the voltage range between 1 and 4 V at 30 °C by charge and discharge.

Fabrication Full Cell. The full cells were fabricated using commercial hard carbon (Kureha) as the anode electrode. The hard carbon was heated at 1000 °C for 2 h in Ar to remove adhered water and air-oxidized substance on the surface of hard carbon particles. The hard carbon electrode was fabricated in the same way and ratio with Cu₂P₂O₇ electrode except Cu foil. To minimize the irreversibility of hard carbon, the hard carbon electrode was presodiated through direct contact with Na metal in 1 M NaPF₆ in DMC:EC:FEC (49:49:2 v/v/v) electrolyte. Finally, R2032 coin-type full cells were assembled with the Cu₂P₂O₇ cathode and presodiated hard carbon anode electrodes (capacity ratio of negative and positive electrodes to be ~1.2) in an Ar glovebox.

Computational Details. Through Vienna Ab Initio Simulation Package (VASP), we performed density functional theory (DFT) calculations⁶⁸ with projector-augmented wave (PAW) pseudo potentials⁶⁹ and a plane-wave basis set. For the exchange-correlation functional, we applied Perdew–Burke–Ernzerhof (PBE) parametrization and the generalized gradient approximation (GGA).^{70,71} For these calculations, an energy cutoff is 520 eV and the remaining force is converged to less than 0.02 eV Å⁻¹ per unit cell. We used the

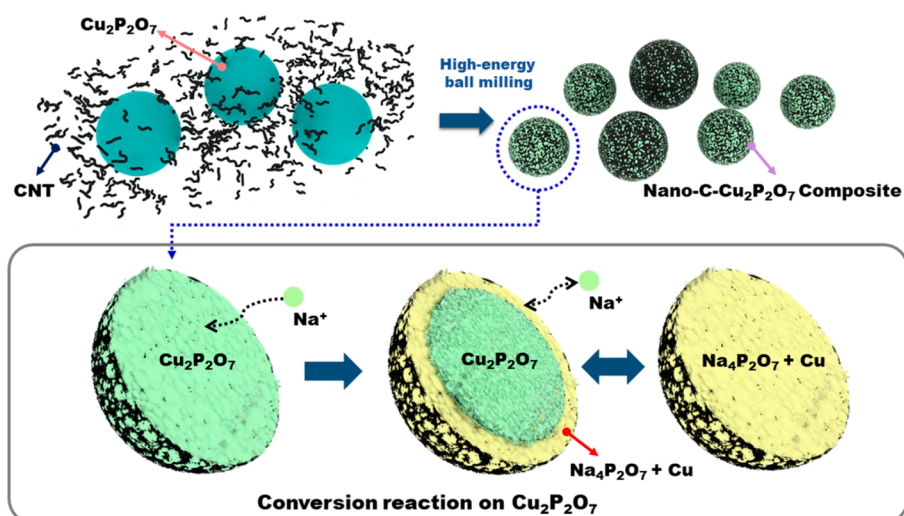


Figure 9. Scheme of the conversion reaction mechanism of the nano-C-Cu₂P₂O₇ during charge/discharge process.

detailed parameters reported at the Materials Project⁷² for the calculation, such as *U* values of compounds.

ASSOCIATED CONTENT

Supporting Information

The Supporting Information is available free of charge on the ACS Publications website at DOI: 10.1021/acsnano.9b05635.

Thermogravimetric analysis (TGA), Raman spectroscopy, X-ray diffraction and SEM images, EIS measurement, electrochemical properties of pristine nano-C-Cu₂P₂O₇, SEM and TEM image after cycling, formation energy table, and lattice parameters of pristine Cu₂P₂O₇ table (PDF)

AUTHOR INFORMATION

Corresponding Authors

*E-mail: smyung@sejong.ac.kr.

*E-mail: jongsoonkim@sejong.ac.kr.

ORCID

Seung-Taek Myung: 0000-0001-6888-5376

Jongsoon Kim: 0000-0002-4122-4874

Author Contributions

#Yongseok Lee and Jung-Keun Yoo contributed equally.

Notes

The authors declare no competing financial interest.

ACKNOWLEDGMENTS

This research was supported by the Radiation Technology R&D program of the National Research Foundation of Korea funded by the Ministry of Science and ICT of Korea (NRF-2019M2A2A6A05102365), International Research & Development Program of the National Research Foundation of Korea funded by the Ministry of Science and ICT of Korea (NRF-2018K2A9A2A12000230), General Research Program of the National Research Foundation of Korea funded by the Ministry of Science and ICT of Korea (NRF-2019R1F1A1063415), Global Research Development Center (GRDC) program of the National Research Foundation of Korea funded by the Ministry of Science and ICT of Korea (NRF-2018K1A4A3A01064272), and by the Research Fund

(PNK6080) of the Korea Institute of Materials Science (KIMS) of the Republic of Korea.

REFERENCES

- (1) Kang, K. S.; Meng, Y. S.; Breger, J.; Grey, C. P.; Ceder, G. Electrodes with High Power and High Capacity for Rechargeable Lithium Batteries. *Science* **2006**, *311*, 977–980.
- (2) Armand, M.; Tarascon, J. M. Building Better Batteries. *Nature* **2008**, *451*, 652–657.
- (3) Palacin, M. R. Recent Advances in Rechargeable Battery Materials: A Chemist's Perspective. *Chem. Soc. Rev.* **2009**, *38*, 2565–2575.
- (4) Kang, B.; Ceder, G. Battery Materials for Ultrafast Charging and Discharging. *Nature* **2009**, *458*, 190–193.
- (5) Scrosati, B.; Garche, J. Lithium Batteries: Status, Prospects and Future. *J. Power Sources* **2010**, *195*, 2419–2430.
- (6) Hu, P.; Zhu, T.; Wang, X.; Wei, X.; Yan, M.; Li, J.; Luo, W.; Yang, W.; Zhang, W.; Zhou, L.; Zhou, Z.; Mai, L. Highly Durable Na₂V₆O₁₆•1.63H₂O Nanowire Cathode for Aqueous Zinc-Ion Battery. *Nano Lett.* **2018**, *18*, 1758–1763.
- (7) Hu, L.; Zheng, S.; Cheng, S.; Chen, Z.; Huang, B.; Liu, Q.; Chen, Q. Micro/Nano-Structured Ag Coated VPO₄/C as a High-Performance Anode Material for Lithium-Ion Batteries. *Mater. Lett.* **2019**, *246*, 40–44.
- (8) Kim, J.; Kim, H.; Kang, K. Surface-Modified Spinel LiNi_{0.5}Mn_{1.5}O₄ for Li-Ion Batteries. *Han'guk Seramik Hakhoechi* **2018**, *55*, 21–35.
- (9) Park, J. S.; Kim, J.; Park, W. B.; Sun, Y. K.; Myung, S. T. Effect of Mn in Li₃V_{2-x}Mn_x(PO₄)₃ as High Capacity Cathodes for Lithium Batteries. *ACS Appl. Mater. Interfaces* **2017**, *9*, 40307–40316.
- (10) Nitta, N.; Wu, F. X.; Lee, J. T.; Yushin, G. Li-Ion Battery Materials: Present and Future. *Mater. Today* **2015**, *18*, 252–264.
- (11) Goriparti, S.; Miele, E.; De Angelis, F.; Di Fabrizio, E.; Zaccaria, R. P.; Capiglia, C. Review on Recent Progress of Nanostructured Anode Materials for Li-Ion Batteries. *J. Power Sources* **2014**, *257*, 421–443.
- (12) Yang, H. W.; Lee, D. I.; Kang, N.; Yoo, J. K.; Myung, S. T.; Kim, J.; Kim, S. J. Highly Enhancement of the SiO_x Nanocomposite through Ti-Doping and Carbon-Coating for High-Performance Li-Ion battery. *J. Power Sources* **2018**, *400*, 613–620.
- (13) Tarascon, J. M.; Armand, M. Issues and Challenges Facing Rechargeable Lithium Batteries. *Nature* **2001**, *414*, 359–367.
- (14) Fu, S. D.; Ni, J. F.; Xu, Y.; Zhang, Q.; Li, L. Hydrogenation Driven Conductive Na₂Ti₃O₇ Nanoarrays as Robust Binder-Free Anodes for Sodium-Ion Batteries. *Nano Lett.* **2016**, *16*, 4544–4551.

- (15) Mei, Y. N.; Huang, Y. H.; Hu, X. L. Nanostructured Ti-Based Anode Materials for Na-Ion Batteries. *J. Mater. Chem. A* **2016**, *4*, 12001–12013.
- (16) Moreau, P.; Guyomard, D.; Gaubicher, J.; Boucher, F. Structure and Stability of Sodium Intercalated Phases in Olivine FePO_4 . *Chem. Mater.* **2010**, *22*, 4126–4128.
- (17) Lee, K. T.; Ramesh, T. N.; Nan, F.; Botton, G.; Nazar, L. F. Topochemical Synthesis of Sodium Metal Phosphate Olivines for Sodium-Ion Batteries. *Chem. Mater.* **2011**, *23*, 3593–3600.
- (18) Barpanda, P.; Ye, T.; Nishimura, S.; Chung, S. C.; Yamada, Y.; Okubo, M.; Zhou, H. S.; Yamada, A. Sodium Iron Pyrophosphate: A Novel 3.0 V Iron-Based Cathode for Sodium-Ion Batteries. *Electrochem. Commun.* **2012**, *24*, 116–119.
- (19) Hwang, J. Y.; Kim, J.; Yu, T. Y.; Sun, Y. K. A New P2-Type Layered Oxide Cathode with Extremely High Energy Density for Sodium-Ion Batteries. *Adv. Energy Mater.* **2019**, *9*, 10.
- (20) Hu, Z.; Liu, Q.; Chou, S.-L.; Dou, S.-X. Advances and Challenges in Metal Sulfides/Selenides for Next-Generation Rechargeable Sodium-Ion Batteries. *Adv. Mater.* **2017**, *29*, 1700606.
- (21) Jo, C. H.; Jo, J. H.; Myung, S. T. Confinement of Nanosized Tin(IV) Oxide Particles on rGO Sheets and Its Application to Sodium-Ion Full Cells as a High Capacity Anode Material. *J. Alloys Compd.* **2018**, *731*, 339–346.
- (22) Kim, J.; Kim, H.; Kang, K. Conversion-Based Cathode Materials for Rechargeable Sodium Batteries. *Adv. Energy Mater.* **2018**, *8*, 1702646.
- (23) Wang, L. P.; Yu, L. H.; Wang, X.; Srinivasan, M.; Xu, Z. C. J. Recent Developments in Electrode Materials for Sodium-Ion Batteries. *J. Mater. Chem. A* **2015**, *3*, 9353–9378.
- (24) Song, W. X.; Ji, X. B.; Wu, Z. P.; Zhu, Y. R.; Yang, Y. C.; Chen, J.; Jing, M. J.; Li, F. Q.; Banks, C. E. First Exploration of Na-Ion Migration Pathways in the NASICON Structure $\text{Na}_3\text{V}_2(\text{PO}_4)_3$. *J. Mater. Chem. A* **2014**, *2*, 5358–5362.
- (25) Yabuuchi, N.; Kajiyama, M.; Iwatate, J.; Nishikawa, H.; Hitomi, S.; Okuyama, R.; Usui, R.; Yamada, Y.; Komaba, S. P2-type $\text{Na}_x[\text{Fe}_{1/2}\text{Mn}_{1/2}]\text{O}_2$ Made from Earth-Abundant Elements for Rechargeable Na Batteries. *Nat. Mater.* **2012**, *11*, 512–517.
- (26) Sun, X.; Jin, Y.; Zhang, C. Y.; Wen, J. W.; Shao, Y.; Zang, Y.; Chen, C. H. Na $[\text{Ni}_{0.4}\text{Fe}_{0.2}\text{Mn}_{0.4-x}\text{Ti}_x]\text{O}_2$: a Cathode of High Capacity and Superior Cyclability for Na-Ion Batteries. *J. Mater. Chem. A* **2014**, *2*, 17268–17271.
- (27) Lv, J.; Yu, C. Q.; Guo, Y.; Bian, Z.; Yang, L.; Chen, Y. P.; Tang, X. F.; Zhang, W. Y.; Qian, Y. J.; Huang, Y. L.; Wang, X. P.; Chen, J. S.; Chen, Z. M.; Qi, L.; Li, L. M.; China Kadoorie, B. Adherence to Healthy Lifestyle and Cardiovascular Diseases in the Chinese Population. *J. Am. Coll. Cardiol.* **2017**, *69*, 1116–1125.
- (28) Kim, J.; Seo, D. H.; Kim, H.; Park, I.; Yoo, J. K.; Jung, S. K.; Park, Y. U.; Goddard, W. A.; Kang, K. Unexpected Discovery of Low-Cost Maricite NaFePO_4 as a High-Performance Electrode for Na-Ion Batteries. *Energy Environ. Sci.* **2015**, *8*, 540–545.
- (29) Zhou, H. J.; Tian, Z. R.; Ang, S. S. Improving the cycling stability of $\text{Na}_3\text{V}_2(\text{PO}_4)_3$ Nanoparticle in Aqueous Sodium Ion Batteries by Introducing Carbon Support. *Mater. Renew. Sustain. Energy* **2016**, *5*.
- (30) Ye, Z.; Zhao, X.; Li, S. D.; Wu, S. Q.; Wu, P.; Nguyen, M. C.; Guo, J. H.; Mi, J. X.; Gong, Z. L.; Zhu, Z. Z.; Yang, Y.; Wang, C. Z.; Ho, K. M. Robust Diamond-Like Fe-Si Network in the Zero-Strain $\text{Na}_x\text{FeSiO}_4$ Cathode. *Electrochim. Acta* **2016**, *212*, 934–940.
- (31) Hwang, J. Y.; Yoon, C. S.; Belharouak, I.; Sun, Y. K. A Comprehensive Study of the Role of Transition Metals in O3-Type Layered $\text{Na}[\text{Ni}_x\text{Co}_y\text{Mn}_z]\text{O}_2$ ($x = 1/3, 0.5, 0.6, \text{ and } 0.8$) Cathodes for Sodium-Ion Batteries. *J. Mater. Chem. A* **2016**, *4*, 17952–17959.
- (32) Kim, H.; Shakoor, R. A.; Park, C.; Lim, S. Y.; Kim, J. S.; Jo, Y. N.; Cho, W.; Miyasaka, K.; Kahraman, R.; Jung, Y.; Choi, J. W. $\text{Na}_2\text{FeP}_2\text{O}_7$ as a Promising Iron-Based Pyrophosphate Cathode for Sodium Rechargeable Batteries: A Combined Experimental and Theoretical Study. *Adv. Funct. Mater.* **2013**, *23*, 1147–1155.
- (33) Guntlin, C. P.; Zund, T.; Kravchyk, K. V.; Worle, M.; Bodnarchuk, M. I.; Kovalenko, M. V. Nanocrystalline FeF_3 and MF_2 ($\text{M} = \text{Fe, Co, and Mn}$) from Metal Trifluoroacetates and Their Li(Na)-Ion Storage Properties. *J. Mater. Chem. A* **2017**, *5*, 7383–7393.
- (34) Dambournet, D.; Chapman, K. W.; Duttine, M.; Borkiewicz, O.; Chupas, P. J.; Groult, H. Lithium Insertion Mechanism in Iron-Based Oxyfluorides with Anionic Vacancies Probed by PDF Analysis. *ChemistryOpen* **2015**, *4*, 443–447.
- (35) Kim, J.; Kim, H.; Park, I.; Park, Y. U.; Yoo, J. K.; Park, K. Y.; Lee, S.; Kang, K. LiFePO_4 with an Alluaudite Crystal Structure for Lithium Ion Batteries. *Energy Environ. Sci.* **2013**, *6*, 830–834.
- (36) Park, K. Y.; Park, I.; Kim, H.; Lim, H. D.; Hong, J.; Kim, J.; Kang, K. Anti-Site Reordering in LiFePO_4 : Defect Annihilation on Charge Carrier Injection. *Chem. Mater.* **2014**, *26*, 5345–5351.
- (37) Liu, H. W.; Ji, P. Y.; Han, X. Y. Rheological Phase Synthesis of Nanosized $\alpha\text{-LiFeO}_2$ with Higher Crystallinity Degree for Cathode Material of Lithium-Ion Batteries. *Mater. Chem. Phys.* **2016**, *183*, 152–157.
- (38) Ko, W.; Yoo, J.-K.; Park, H.; Lee, Y.; Kim, H.; Oh, Y.; Myung, S.-T.; Kim, J. Development of $\text{Na}_2\text{FePO}_4\text{F}$ /Conducting-Polymer Composite as an Exceptionally High Performance Cathode Material for Na-Ion Batteries. *J. Power Sources* **2019**, *432*, 1–7.
- (39) Ko, W.; Park, T.; Park, H.; Lee, Y.; Lee, K. E.; Kim, J. $\text{Na}_{0.97}\text{KFe}(\text{SO}_4)_2$: an Iron-Based Sulfate Cathode Material with Outstanding Cyclability and Power Capability for Na-Ion Batteries. *J. Mater. Chem. A* **2018**, *6*, 17095–17100.
- (40) Yoo, J. K.; Kim, J.; Jung, Y. S.; Kang, K. Scalable Fabrication of Silicon Nanotubes and their Application to Energy Storage. *Adv. Mater.* **2012**, *24*, 5452–5456.
- (41) Voronina, N.; Jo, J. H.; Choi, J. U.; Jo, C.-H.; Kim, J.; Myung, S.-T. Nb-Doped Titanium Phosphate for Sodium Storage: Electrochemical Performance and Structural Insights. *J. Mater. Chem. A* **2019**, *7*, 5748–5759.
- (42) Karaphun, A.; Chirawatkul, P.; Maensiri, S.; Swatsitang, E. Influence of Calcination Temperature on the Structural, Morphological, Optical, Magnetic and Electrochemical Properties of $\text{Cu}_2\text{P}_2\text{O}_7$ Nanocrystals. *J. Sol-Gel Sci. Technol.* **2018**, *88*, 407–421.
- (43) Pogorzelec-Glaser, K.; Pietraszko, A.; Hilczer, B.; Polomska, M. Structure and Phase Transitions in $\text{Cu}_2\text{P}_2\text{O}_7$. *Phase Transitions* **2006**, *79*, 535–544.
- (44) Le, S. N.; Navrotsky, A.; Pralong, V. Energetics of Copper Diphosphates - $\text{Cu}_2\text{P}_2\text{O}_7$ and $\text{Cu}_3(\text{P}_2\text{O}_6\text{OH})_2$. *Solid State Sci.* **2008**, *10*, 761–767.
- (45) Chen, R. J.; Luo, R.; Huang, Y. X.; Wu, F.; Li, L. Advanced High Energy Density Secondary Batteries with Multi-Electron Reaction Materials. *Adv. Sci.* **2016**, *3*, 39.
- (46) Klein, F.; Jache, B.; Bhide, A.; Adelhelm, P. Conversion Reactions for Sodium-Ion Batteries. *Phys. Chem. Chem. Phys.* **2013**, *15*, 15876–15887.
- (47) Hu, Z.; Liu, Q. N.; Chou, S. L.; Dou, S. X. Advances and Challenges in Metal Sulfides/Selenides for Next-Generation Rechargeable Sodium-Ion Batteries. *Adv. Mater.* **2017**, *29*, 24.
- (48) Ali, G.; Oh, S. H.; Kim, S. Y.; Kim, J. Y.; Cho, B. W.; Chung, K. Y. An Open-Framework Iron Fluoride and Reduced Graphene Oxide Nanocomposite as a High-Capacity Cathode Material for Na-Ion Batteries. *J. Mater. Chem. A* **2015**, *3*, 10258–10266.
- (49) Ma, D.-l.; Wang, H.-g.; Li, Y.; Xu, D.; Yuan, S.; Huang, X.-l.; Zhang, X.-b.; Zhang, Y. *In Situ* Generated FeF_3 in Homogeneous Iron Matrix toward High-Performance Cathode Material for Sodium-Ion Batteries. *Nano Energy* **2014**, *10*, 295–304.
- (50) Zhou, Y.-N.; Sina, M.; Pereira, N.; Yu, X.; Amatucci, G. G.; Yang, X.-Q.; Cosandey, F.; Nam, K.-W. $\text{FeO}_{0.7}\text{F}_{1.3}/\text{C}$ Nanocomposite as a High-Capacity Cathode Material for Sodium-Ion Batteries. *Adv. Funct. Mater.* **2015**, *25*, 696–703.
- (51) Choi, J. U.; Kim, J.; Hwang, J.-Y.; Jo, J. H.; Sun, Y.-K.; Myung, S.-T. $\text{K}_{0.54}[\text{Co}_{0.5}\text{Mn}_{0.5}]\text{O}_2$: New Cathode with High Power Capability for Potassium-Ion Batteries. *Nano Energy* **2019**, *61*, 284–294.
- (52) Yao, X.; Zhu, Z.; Li, Q.; Wang, X.; Xu, X.; Meng, J.; Ren, W.; Zhang, X.; Huang, Y.; Mai, L. 3.0 V High Energy Density Symmetric Sodium-Ion Battery: $\text{Na}_4\text{V}_2(\text{PO}_4)_3$ Parallel $\text{Na}_3\text{V}_2(\text{PO}_4)_3$. *ACS Appl. Mater. Interfaces* **2018**, *10*, 10022–10028.

- (53) Su, D.; Ahn, H.-J.; Wang, G. β -MnO₂ Nanorods with Exposed Tunnel Structures as High-Performance Cathode Materials for Sodium-Ion Batteries. *NPG Asia Mater.* **2013**, *5*, e70–e70.
- (54) Liu, M.; Wang, X.; Wei, S.; Hu, H.; Zhang, R.; Liu, L. Cr-Doped Fe₂F₃·H₂O with Open Framework Structure as a High Performance Cathode Material of Sodium-Ion Batteries. *Electrochim. Acta* **2018**, *269*, 479–489.
- (55) Cho, M. K.; Jo, J. H.; Choi, J. U.; Kim, J.; Yashiro, H.; Yuan, S.; Shi, L. Y.; Sun, Y. K.; Myung, S. T. Tunnel-Type Beta-FeOOH Cathode Material for High Rate Sodium Storage via a New Conversion Reaction. *Nano Energy* **2017**, *41*, 687–696.
- (56) Shen, Y.; Wang, X.; Hu, H.; Jiang, M.; Bai, Y.; Yang, X.; Shu, H. Sheet-like Structure FeF₃/graphene Composite as Novel Cathode Material for Na Ion Batteries. *RSC Adv.* **2015**, *5*, 38277–38282.
- (57) Liu, H.; Zhou, H.; Chen, L.; Tang, Z.; Yang, W. Electrochemical Insertion/Deinsertion of Sodium on NaV₆O₁₅ Nanorods as Cathode Material of Rechargeable Sodium-Based Batteries. *J. Power Sources* **2011**, *196*, 814–819.
- (58) Yabuuchi, N.; Hara, R.; Kubota, K.; Paulsen, J.; Kumakura, S.; Komaba, S. A new electrode material for rechargeable sodium batteries: P2-type Na_{2/3}[Mg_{0.28}Mn_{0.72}]O₂ with Anomalously High Reversible Capacity. *J. Mater. Chem. A* **2014**, *2*, 16851–16855.
- (59) Mahadi, N. B.; Park, J.-S.; Park, J.-H.; Chung, K. Y.; Yi, S. Y.; Sun, Y.-K.; Myung, S.-T. Vanadium Dioxide – Reduced Graphene Oxide Composite as Cathode Materials for Rechargeable Li and Na Batteries. *J. Power Sources* **2016**, *326*, 522–532.
- (60) Yoshida, J.; Guerin, E.; Arnault, M.; Constantin, C.; de Boisse, B. M.; Carlier, D.; Guignard, M.; Delmas, C. New P2-Na_{0.70}Mn_{0.60}Ni_{0.30}Co_{0.10}O₂ Layered Oxide as Electrode Material for Na-Ion Batteries. *J. Electrochem. Soc.* **2014**, *161*, A1987–A1991.
- (61) Hu, Z.; Zhu, Z.; Cheng, F.; Zhang, K.; Wang, J.; Chen, C.; Chen, J. Pyrite FeS₂ for High-Rate and Long-Life Rechargeable Sodium Batteries. *Energy Environ. Sci.* **2015**, *8*, 1309–1316.
- (62) Li, L.; Meng, F.; Jin, S. High-Capacity Lithium-Ion Battery Conversion Cathodes Based on Iron Fluoride Nanowires and Insights into the Conversion Mechanism. *Nano Lett.* **2012**, *12*, 6030–6037.
- (63) Liu, X.; Liu, H.; Zhao, Y.; Dong, Y.; Fan, Q.; Kuang, Q. Synthesis of the Carbon-Coated Nanoparticle Co₉S₈ and Its Electrochemical Performance as an Anode Material for Sodium-Ion Batteries. *Langmuir* **2016**, *32*, 12593–12602.
- (64) Wang, Y.; Wang, Y.; Hosono, E.; Wang, K.; Zhou, H. The Design of a LiFePO₄/Carbon Nanocomposite with a Core-Shell Structure and its Synthesis by an *In Situ* Polymerization Restriction Method. *Angew. Chem., Int. Ed.* **2008**, *47*, 7461–7465.
- (65) Lyu, H.; Gao, B.; He, F.; Ding, C.; Tang, J.; Crittenden, J. C. Ball-Milled Carbon Nanomaterials for Energy and Environmental Applications. *ACS Sustainable Chem. Eng.* **2017**, *5*, 9568–9585.
- (66) Rodriguez, J. A.; Hanson, J. C.; Stacchiola, D.; Senanayake, S. D. *In Situ*/Operando Studies for the Production of Hydrogen through the Water-Gas Shift on Metal Oxide Catalysts. *Phys. Chem. Chem. Phys.* **2013**, *15*, 12004–12025.
- (67) Fox, E. B.; Velu, S.; Engelhard, M. H.; Chin, Y.-H.; Miller, J. T.; Kropf, J.; Song, C. Characterization of CeO₂-Supported Cu–Pd Bimetallic Catalyst for the Oxygen-Assisted Water–Gas Shift Reaction. *J. Catal.* **2008**, *260*, 358–370.
- (68) Kresse, G.; Furthmüller, J. Efficiency of *Ab Initio* Total Energy Calculations for Metals and Semiconductors Using a Plane-Wave Basis Set. *Comput. Mater. Sci.* **1996**, *6*, 15–50.
- (69) Blochl, P. E. Projector Augmented-Wave Method. *Phys. Rev. B: Condens. Matter Mater. Phys.* **1994**, *50*, 17953–17979.
- (70) Perdew, J. P.; Burke, K.; Ernzerhof, M. Generalized Gradient Approximation Made Simple. *Phys. Rev. Lett.* **1996**, *77*, 3865–3868.
- (71) Anisimov, V. I.; Aryasetiawan, F.; Lichtenstein, A. I. First-Principles Calculations of the Electronic Structure and Spectra of Strongly Correlated Systems: The LDA+U Method. *J. Phys.: Condens. Matter* **1997**, *9*, 767–808.
- (72) Jain, A.; Ong, S. P.; Hautier, G.; Chen, W.; Richards, W. D.; Dacek, S.; Cholia, S.; Gunter, D.; Skinner, D.; Ceder, G.; Persson, K. A. Commentary: The Materials Project: A Materials Genome Approach to Accelerating Materials Innovation. *APL Mater.* **2013**, *1*, 11.